A Method for Selecting SAR Interferometric Pairs Based on Coherence Spectral Clustering

Yuan Wang, Huaping Xu, *Member, IEEE*, Guobing Zeng, Wei Liu, *Senior Member, IEEE,* Shuo Li, Chunsheng Li

***Abstract*—To achieve accurate interferometric synthetic aperture radar (SAR) phase estimation, it is essential to select appropriate high-coherence interferometric pairs from massive SAR single-look complex (SLC) image data. The selection should include as many high-coherence interferometric pairs as possible while avoiding low-coherence pairs. By combining coherence and spectral clustering, a novel selection method for SAR interferometric pairs is proposed in this paper. The proposed method can be adopted to classify SAR SLC images into different clusters, where the total coherence of interferometric pairs in the same cluster is maximized while that among the different clusters is minimized. This is implemented by averaging the coherence matrices of representative pixels to construct an adjacency matrix and performing eigenvalue decomposition for estimating the number of clusters. The effectiveness of the proposed method is demonstrated using 33 TerraSAR-X and 38 dual-polarization Sentinel-1A data samples, yielding improved topography and deformation monitoring results.**

***Index Terms*—Synthetic aperture radar (SAR), interferometric pair selection, coherence, spectral clustering, interferometric phase estimation accuracy.**

I. Introduction

Synthetic aperture radar (SAR) can obtain high-resolution images even under adverse weather circumstances. As a successful application that combines traditional SAR technology with interferometry, the interferometric synthetic aperture radar (InSAR) can retrieve digital elevation model (DEM) and surface deformation data [1]. The interferometric phase is related to the slant range distance difference between the primary and secondary SAR single-look complex (SLC) images. A high-quality interferometric phase is essential to retrieve DEM and surface deformation data [2]. With an increasing number of SAR satellites in orbit, an unprecedented number of SAR SLC images are now available. They provide more samples for interferometric phase estimation, thus facilitating estimation accuracy enhancement. Therefore, the Multi-Channel InSAR (MCInSAR) [3], [4] and Multi-Temporal InSAR (MTInSAR) [5], [6] techniques have recently received widespread attention.

In the MCInSAR technique, multiple interferometric pairs are employed to resolve the contradiction between coherence and ambiguity height [4], [7], which can provide more accurate DEM data than the traditional single-channel InSAR technique, while in the MTInSAR technique, multiple interferometric pairs at different times are utilized to estimate the ground displacement time series [8], [9]. Usually, two SAR SLC images with coherence greater than a certain threshold are considered sufficiently coherent and can be used for interferometry [3]. In this paper, interferometric pairs with a coherence value greater than 0.55 are considered high-coherence interferometric pairs.

To reduce the number of invalid pixels in DEM results, MCInSAR aims to select high-coherence interferometric pairs by restricting spatial-temporal baseline or pixel-by-pixel dynamic selection [7]. MTInSAR techniques can be divided into two categories. In one category, all possible interferometric pairs are used, including SqueeSAR [8], Component extrAction and sElection SAR (CAESAR) [9] and Eigendecomposition-based Maximum-likelihood-estimator of Interferometric phase (EMI) [10], etc.; in the other category, only some high-coherence interferometric pairs are selected, such as the Small BAseline Subset (SBAS) technique [11]. Compared to the first category, low-coherence interferometric pairs are removed in the second category. This can avoid the adverse effect of low-coherence interferometric pairs [12], [13] and reduce the computational burden [14]. Therefore, many modified SBAS methods with different selection strategies have been proposed [15]-[17].

The Cramer–Rao lower bound (CRLB) for interferometric phase estimation is closely related to the coherence matrix of SAR SLC images [18]. The larger the number of higher-coherence interferometric pairs selected, the more accurate interferometric phase estimation can be theoretically achieved. Inappropriate selection of low-coherence interferometric pairs can result in a low-quality coherence matrix, which can reduce the phase estimation accuracy. Therefore, how to select high-coherence interferometric pairs and remove low-coherence ones is vital to both the MCInSAR and MTInSAR techniques.

Permanent scatterer interferometry (PS-InSAR) [19] focuses on identifying persistent scatterers (PSs) and measuring their displacements, in which a common primary SAR SLC image is employed to form interferometric pairs with large spatial-temporal baselines. To avoid selecting pairs with significant spatial and temporal decorrelation, the SBAS technique was

Manuscript received March 16, 2023; revised 2 July 2023, 13 September and 19 October 2023; accepted 21 October 2023. This work was supported by the National Natural Science Foundation of China under grant U2241202.

Y. Wang, H. Xu, G. Zeng and C. Li are with the School of Electronic and Information Engineering, Beihang University, Beijing 100191, China (e-mail: wyuan@buaa.edu.cn, xuhuaping@buaa.edu.cn, zengguobing@buaa.edu.cn, lics@buaa.edu.cn).

W. Liu is with the School of Electronic Engineering and Computer Science, Queen Mary University of London, London E1 4NS, UK (e-mail: w.liu@qmul.ac.uk).

S. Li is with the Nanjing Research Institute of Electronics Technology, Nanjing 211113, China (shuo201@buaa.edu.cn).

proposed by empirically setting a spatial-temporal baseline threshold [11]. This threshold is not adaptively adjusted according to terrain characteristics. In addition, the spatial-temporal baseline cannot completely represent the coherence of a given interferometric pair. Therefore, the SBAS technique can hardly ensure that all the selected interferometric pairs have high coherence or that all high-coherence interferometric pairs have been selected.

Aiming to overcome the limitations of a fixed threshold, adaptive threshold methods have emerged. In [15] and [20], the threshold was adjusted according to the coherence of the analyzed pixels. High-coherence interferometric pairs were adaptively selected for each analyzed pixel instead of the whole set of pixels. The spatial-temporal baseline threshold of each pixel was estimated by maximizing the deformation estimation accuracy while maintaining high coherence [21]. Interferometric pairs, at three times the number of SAR SLC images, were selected based on the coherence of high signal-to-noise ratio (SNR) pixels in the featured region [22]. In [23], candidate interferometric pairs were chosen considering a spatial-temporal baseline threshold. Their average coherence was utilized to estimate a coherence threshold by minimizing the relative deformation error. These methods, in general, involve the selection of interferometric pairs based on thresholds, such as the spatial-temporal baseline or coherence. However, a high threshold can result in some relatively high-coherence pairs not being selected, while a low threshold can lead to incorrectly selecting low-coherence pairs. Therefore, these threshold-based methods suffer from a common problem: it is relatively difficult to define an appropriate threshold that can guarantee that all high-coherence pairs are selected and that all selected pairs exhibit high coherence.

To avoid determining a threshold, optimization-based methods have been proposed. Pepe et al. introduced a cost function to describe the overall coherence of interferometric pairs, which was then minimized through a simulated annealing algorithm [24]. Interferometric pairs with large spatial-temporal baselines but high coherence could likely be missed because triangulation is needed when constructing the interferometric pair network. In addition, certain graph theory algorithms, such as Dijkstra's shortest-path algorithm [25], the all-pairs-shortest-path (APSP) algorithm [26] and the minimum spanning tree (MST) algorithm [27], have been utilized to select interferometric pairs. However, the APSP algorithm is not recommended for data acquired over high-coherence areas because abrupt coherence loss rarely occurs [28]; MST-based selection methods require full connection of images to ensure connectivity. As a result, low-coherence interferometric pairs likely occur in the network, which leads to negative effects on the subsequent processing procedure [27]. Smittarello et al. proposed directly fitting the coherence of interferometric pairs and restricting the use of each image as either a primary or secondary image, and a graph theory method was then applied to limit the total number of selected pairs [29]. Due to the limited number of interferometric pairs in each image, some high-coherence ones could be missed. These methods usually impose certain constraints on the selection of interferometric pairs, resulting in limited adaptability to data with different coherence distributions. Furthermore, pairs with relatively high coherence might be missed, or those with low coherence might be wrongly selected as a result of inappropriate constraints.

Without imposing such constraints, a spectral clustering algorithm can be used to identify sample spaces of any shapes and converge to the global optimal solution [30]. Inspired by the idea of spectral clustering, through combination with coherence, a novel method for the selection of interferometric pairs is proposed in this paper. In the proposed method, high-coherence pairs are selected at the preprocessing step, and these pairs can be quickly and effectively identified. Moreover, owing to the adaptive estimation of the number of clusters, the proposed method is more adaptable to data with different coherence distributions. The selected results can be used not only for deformation monitoring with the MTInSAR technique but also for exploring multibaseline interferometric phase filtering, unwrapping and elevation reconstruction methods in the MCInSAR technique.

First, a set of representative pixels is chosen, and their coherence matrices are calculated through the identification of statistically homogeneous pixels (SHPs). Then, the number of clusters is estimated via eigenvalue decomposition of the coherence matrix of each representative pixel. Finally, the coherence matrix of SAR SLC images is employed as the adjacency matrix to select interferometric pairs. The total coherence of the interferometric pairs in the same cluster is maximized, while that among the different clusters is minimized. Therefore, high-coherence interferometric pairs are selected, and low-coherence ones are removed. Therefore, the proposed method can be employed to select pairs with a high-quality coherence matrix to achieve accurate interferometric phase estimation in MCInSAR and MTInSAR.

The remainder of this paper is structured as follows: spectral clustering is briefly introduced in Section II, and the proposed selection method is presented in Section III. The effectiveness of the proposed method is demonstrated in Section IV using two sets of real SAR data from TerraSAR-X and Sentinel-1A. Conclusions are outlined in Section V.

II. SPECTRAL CLUSTERING

Many clustering methods have been proposed over the past few decades. With the use of spectral clustering, based on graph partitioning theory, the challenging clustering problem can be converted into an optimal subgraph partitioning problem. The fundamentals of spectral clustering comprise two parts: adjacency matrix construction and subgraph cut generation [30].

A. Adjacency Matrix Construction

In graph theory, an undirected graph $G=(V,E)$ usually contains the set of points $V=(\upsilon_1,\upsilon_2,\cdots,\upsilon_N)$ and the set of edges E. Regarding the connecting line between any two points υ_i and υ_j in V, ω_{ij} denotes its weight, and $\omega_{ij}=\omega_{ji}$. The adjacency matrix $\mathbf{W}$ encompasses all ω_{ij}, which is greater than 0 and proportional to the similarity

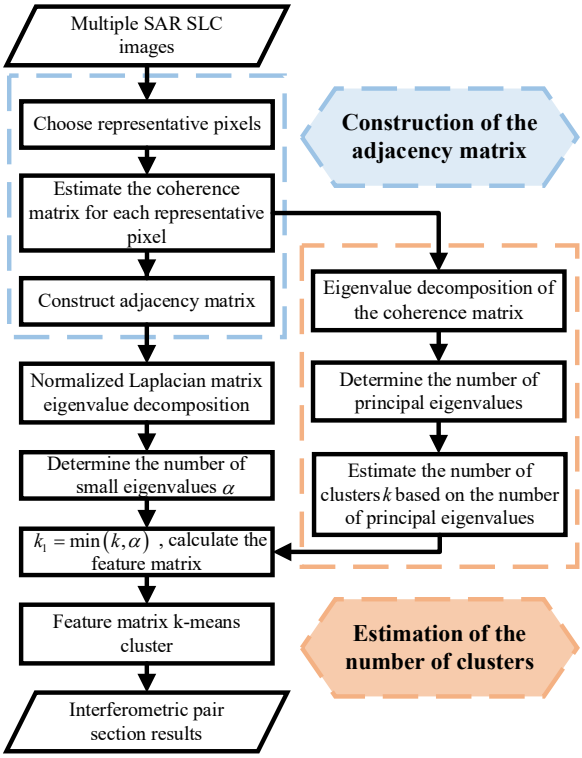

Fig. 1. Interferometric pair selection method based on coherence spectral clustering.

between the two points. Based on the adjacency matrix $\mathbf{W}$, the degree matrix $\mathbf{D}$ and the Laplacian matrix $\mathbf{L}$ can be calculated. $\mathbf{D}$ is a diagonal matrix defined as

$$\mathbf{D} = \begin{bmatrix} d_1 & 0 & \cdots & 0 \\ 0 & d_2 & \cdots & 0 \\ \cdots & \cdots & \cdots & \cdots \\ 0 & 0 & \cdots & d_N \end{bmatrix} \tag{1}$$

where $d_i = \sum_{j=1}^{N} \omega_{ij}, i = 1, \cdots, N$ denotes the total weights of all edges connected to point υ_i, hereafter referred to as the degree of υ_i.

The Laplacian matrix $\mathbf{L} = \mathbf{D} - \mathbf{W}$ is a positive semidefinite symmetric matrix. For any vector $\mathbf{f}$, the following applies:

$$\mathbf{f}^T \mathbf{L} \mathbf{f} = \frac{1}{2} \sum_{i=1, j=1}^{N} \omega_{ij} \left(\mathbf{f}_i - \mathbf{f}_j \right)^2 \tag{2}$$

B. Subgraph Cut Generation

Subgraph cut generation aims at dividing the undirected graph $G = (V, E)$ into k subgraphs $\{A_1, A_2, \cdots A_k\}$, with the total edge weight among the different subgraphs minimized and the total edge weight within each subgraph maximized. The objective function of the normalized cut criterion is [31]:

$$\arg\min_{A_1, A_2, \cdots A_k} \frac{1}{2} \sum_{i=1}^{k} \frac{W(A_i, \bar{A}_i)}{\upsilon ol(A_i)} \tag{3}$$

where $\bar{A}_i$ is the complement of subgraph A_i, $W(A_i, \bar{A}_i)$ is the total edge weight between A_i and $\bar{A}_i$, and $\upsilon ol(A_i)$ is the sum of the degrees of all points in subgraph A_i.

The indicator vector matrix $\mathbf{H}$ is introduced for k subgraphs and satisfies $\mathbf{H}^T \mathbf{L} \mathbf{H} = \mathbf{F}^T \mathbf{D}^{-1/2} \mathbf{L} \mathbf{D}^{-1/2} \mathbf{F}$. It is an NP-hard problem to find $\mathbf{H}$ that satisfies the normalized cut criterion. With the use of the idea of dimensionality reduction, the optimization objective function of the subgraph normalized cut can be transformed into [31]:

$$\arg\min_{\mathbf{F}} tr\left(\mathbf{F}^T \mathbf{D}^{-1/2} \mathbf{L} \mathbf{D}^{-1/2} \mathbf{F} \right) \quad s.t. \quad \mathbf{F}^T \mathbf{F} = \mathbf{I} \tag{4}$$

where $\mathbf{D}^{-1/2} \mathbf{L} \mathbf{D}^{-1/2}$ is the normalized Laplacian matrix.

According to the trace properties, minimizing $tr\left(\mathbf{F}^T \mathbf{D}^{-1/2} \mathbf{L} \mathbf{D}^{-1/2} \mathbf{F} \right)$ is equivalent to finding the k_1 lowest eigenvalues of $\mathbf{D}^{-1/2} \mathbf{L} \mathbf{D}^{-1/2}$. The k_1 eigenvectors are normalized by rows to form an $N \times k_1$ feature matrix $\mathbf{F}$. The k-means clustering technique with k clusters is then applied to the feature matrix $\mathbf{F}$ to obtain k subgraph cut results.

The key points of spectral clustering are the adjacency matrix and the number of clusters. The adjacency matrix contains the edge weights of any two points, which is the foundation for constructing the degree matrix and Laplacian matrix. Therefore, it is essential to construct an adjacency matrix that accurately reflects the similarity between two points. Moreover, the subgraph cut results are directly affected by the number of clusters. The clustering performance can be significantly improved if the number of clusters can be adjusted on the basis of the data.

III. Interferometric Pair Selection Based on Coherence Spectral Clustering

In this section, the proposed SAR interferometric pair selection method based on coherence spectral clustering is introduced, and its flowchart is shown in Fig. 1. In the proposed method, the SAR SLC image and coherence are regarded as point and edge weights, respectively. High-coherence pairs are selected by subgraph cut generation.

First, the adjacency matrix is constructed by coherence estimation. A set of representative pixels is chosen, and the corresponding coherence matrix of each representative pixel is estimated by identifying SHPs. The adjacency matrix is constructed by averaging the coherence matrices of all representative pixels.

Then, the number of clusters is estimated by performing eigenvalue decomposition of the coherence matrix. The number of principal eigenvalues of each representative pixel is determined by eigenvalue decomposition. To improve robustness, the number of clusters k is determined based on the mode of the number of principal eigenvalues of all representative pixels.

Finally, subgraph cut generation is achieved by minimizing the optimization objective function. The normalized Laplacian matrix is constructed based on the adjacency matrix, and eigenvalue decomposition of the normalized Laplacian matrix is then performed to obtain the first α low eigenvalues. The

reduced dimension is determined as $k_1 = \min(k, \alpha)$, and the dimension of the feature matrix $\mathbf{F}$ is $N \times k_1$. The k-means clustering technique with k clusters is applied to $\mathbf{F}$ for obtaining the selection results.

In the following, details are provided for constructing the adjacency matrix and estimating the number of clusters.

A. Construction of the Adjacency Matrix

In the proposed method, the coherence matrix is employed as the adjacency matrix $\mathbf{W}$. Its element ω_{ij} denotes the coherence between the ith and jth SAR SLC images, with $\omega_{ij} = \omega_{ji}$.

The coherence of two SAR SLC images can usually be estimated by averaging the coherence values of all pixels over the entire image [2]. With increasing number of SAR SLC images, coherence calculation becomes a computationally intensive and time-consuming task. Therefore, only high-SNR pixels in the featured regions are used [21]. Although this method can provide computational efficiency improvement, its results heavily depend on the selection of featured regions. If the average coherence of the featured regions cannot accurately reflect the overall coherence, the selection results will not be optimal.

To better characterize the overall coherence of two SAR SLC images, it is proposed to choose representative pixels for estimating coherence. Usually, pixels are considered PSs if the number of SHPs is smaller than 8, as determined by the Kolmogorov–Smirnov (KS) test [8]. PSs are not significantly affected by spatial and temporal decorrelation [19], and their coherence cannot accurately represent the overall coherence of an interferometric pair. Therefore, layover, shadow and water body areas are detected first; then, for pixels along the range and azimuth directions with equal intervals, if they are excluded in layover, shadow and water body areas and the number of SHPs is larger than or equal to 8, these pixels are added to the representative pixel set $\delta(p_1, p_2, \cdots, p_M)$. Since there are N SAR SLC images, the dimension of the estimated coherence matrix of each representative pixel is $N \times N$. Finally, the coherence matrix of N SAR SLC images can be estimated by averaging the coherence magnitude of M representative pixels, which is used to construct the $N \times N$ adjacency matrix.

Here, SHPs are identified to improve the accuracy of coherence estimation [8]. For an $A \times A$ window centered on the representative pixels p_m, assume that Q SHPs $p_{m,q}$ $m = 1, 2, \cdots, M$ and $q = 1, 2, \cdots, Q$ can be obtained through the SHP test. These SHPs are independent and identically distributed. The coherence matrix of the representative pixel p_m can be expressed as:

$$\hat{\mathbf{\Gamma}}(p_m) = \frac{1}{Q} \sum_{q=1}^{Q} \mathbf{y}(p_{m,q}) \mathbf{y}(p_{m,q})^H \tag{5}$$

where H denotes the conjugate transpose operation, and the following can be obtained:

$$\mathbf{y}(p_{m,q}) = \left[y_1(p_{m,q}) \quad y_2(p_{m,q}) \quad \cdots \quad y_N(p_{m,q}) \right]^T, \quad m = 1, \cdots M, q = 1, \cdots, Q \tag{6}$$

where T denotes the transpose operation, and $y_i(p_{m,q}), i = 1, 2, \cdots, N$ can be obtained from N SAR SLC images $d_i(p_{m,q}), i = 1, 2, \cdots, N$ by amplitude normalization, expressed as:

$$y_i(p_{m,q}) = d_i(p_{m,q}) / \sqrt{\frac{1}{N} \sum_{i=1}^{N} \left| d_i(p_{m,q}) \right|^2} \tag{7}$$

$\hat{\mathbf{\Gamma}}(p_m)$ contains both coherence magnitude and interferometric phase information. By averaging the coherence magnitude of M representative pixels, $\hat{\mathbf{\Gamma}}_N$ can be obtained, whose entry $\hat{\mathbf{\Gamma}}_N(i, j)$ denotes the coherence between the ith and jth SAR SLC images.

To improve the coherence matrix estimation accuracy, the proposed method can be used to identify SHPs and eliminate pixels in layover, shadow and water body areas. The estimated coherence matrix of N SAR SLC images is then employed as the adjacency matrix, reflecting the similarity between two points in spectral clustering.

B. Estimation of the Number of Clusters

It has been demonstrated that by performing eigenvalue decomposition, multiple scattering mechanisms can be effectively separated and estimated from the coherence matrix [9], [13]. Therefore, in this paper, the number of clusters is estimated by performing eigenvalue decomposition of the coherence matrix of each representative pixel.

The estimated coherence matrix $\hat{\mathbf{\Gamma}}(p_m)$ follows the complex Wishart distribution [9] and is a positive semidefinite Hermitian matrix, which can be decomposed as:

$$\hat{\mathbf{\Gamma}}(p_m) = \mathbf{U} \mathbf{\Lambda} \mathbf{U}^{-1} = \mathbf{U} \mathbf{\Lambda} \mathbf{U}^H = \sum_{i=1}^{N} \lambda_i \mathbf{u}_i \mathbf{u}_i^H \tag{8}$$

where λ_i is a nonnegative eigenvalue that represents the proportion of the ith scattering mechanism in the coherence matrix, and $\mathbf{u}_i$ is the eigenvector corresponding to λ_i. In general, the larger λ_i is, the more dominant the corresponding scattering mechanism.

Generally, the coherence among SAR SLC images with the same dominant scattering mechanism is relatively high [12], [32], so the corresponding SAR SLC images are more likely to be classified into the same cluster. Let the coherence matrix of each cluster at pixel p_m be denoted as $\hat{\mathbf{\Gamma}}_1(p_m) \sim \hat{\mathbf{\Gamma}}_k(p_m)$, and the coherence matrix of SAR SLC images from different clusters be denoted as $\hat{\mathbf{\Gamma}}_{ij}(p_m), i, j = 1, \cdots, k$, where the coherence magnitude of each element is small. Therefore, the estimated coherence matrix $\hat{\mathbf{\Gamma}}(p_m)$ can be expressed as:

$$\begin{aligned}\hat{\boldsymbol{\Gamma}}(p_m)&=\begin{bmatrix}\hat{\boldsymbol{\Gamma}}_1(p_m) & \hat{\boldsymbol{\Gamma}}_{12}(p_m) & \cdots & \hat{\boldsymbol{\Gamma}}_{1k}(p_m)\\ \hat{\boldsymbol{\Gamma}}_{21}(p_m) & \hat{\boldsymbol{\Gamma}}_2(p_m) & \cdots & \hat{\boldsymbol{\Gamma}}_{2k}(p_m)\\ \cdots & \cdots & \cdots & \cdots\\ \hat{\boldsymbol{\Gamma}}_{k1}(p_m) & \hat{\boldsymbol{\Gamma}}_{k2}(p_m) & \cdots & \hat{\boldsymbol{\Gamma}}_k(p_m)\end{bmatrix}\\&=\begin{bmatrix}\hat{\boldsymbol{\Gamma}}_1(p_m) & 0 & \cdots & 0\\ 0 & \hat{\boldsymbol{\Gamma}}_2(p_m) & \cdots & 0\\ \cdots & \cdots & \cdots & \cdots\\ 0 & 0 & \cdots & \hat{\boldsymbol{\Gamma}}_k(p_m)\end{bmatrix}+\\&\quad\begin{bmatrix}0 & \hat{\boldsymbol{\Gamma}}_{12}(p_m) & \cdots & \hat{\boldsymbol{\Gamma}}_{1k}(p_m)\\ \hat{\boldsymbol{\Gamma}}_{21}(p_m) & 0 & \cdots & \hat{\boldsymbol{\Gamma}}_{2k}(p_m)\\ \cdots & \cdots & \cdots & \cdots\\ \hat{\boldsymbol{\Gamma}}_{k1}(p_m) & \hat{\boldsymbol{\Gamma}}_{k2}(p_m) & \cdots & 0\end{bmatrix}\\&=\hat{\boldsymbol{\Gamma}}_A(p_m)+\hat{\boldsymbol{\Gamma}}_B(p_m)\end{aligned}\tag{9}$$

The coherence matrices $\hat{\boldsymbol{\Gamma}}(p_m)$ and $\hat{\boldsymbol{\Gamma}}_1(p_m)\sim\hat{\boldsymbol{\Gamma}}_k(p_m)$ are positive semidefinite Hermitian matrices, so $\hat{\boldsymbol{\Gamma}}_A(p_m)$ is also a positive semidefinite Hermitian matrix [33], which can be decomposed as:

$$\begin{aligned}\hat{\boldsymbol{\Gamma}}_A(p_m)&=\begin{bmatrix}\hat{\boldsymbol{\Gamma}}_1(p_m) & 0 & \cdots & 0\\ 0 & \hat{\boldsymbol{\Gamma}}_2(p_m) & \cdots & 0\\ \cdots & \cdots & \cdots & \cdots\\ 0 & 0 & \cdots & \hat{\boldsymbol{\Gamma}}_k(p_m)\end{bmatrix}\\&=\begin{bmatrix}\mathbf{U}_{A1} & \mathbf{U}_{A2} & \cdots & \mathbf{U}_{Ak}\end{bmatrix}\begin{bmatrix}\boldsymbol{\Lambda}_{A1} & 0 & \cdots & 0\\ 0 & \boldsymbol{\Lambda}_{A2} & \cdots & 0\\ \cdots & \cdots & \cdots & \cdots\\ 0 & 0 & \cdots & \boldsymbol{\Lambda}_{Ak}\end{bmatrix}\begin{bmatrix}\mathbf{U}_{A1}^H\\ \mathbf{U}_{A2}^H\\ \vdots\\ \mathbf{U}_{Ak}^H\end{bmatrix}\\&=\mathbf{U}_{A1}\boldsymbol{\Lambda}_{A1}\mathbf{U}_{A1}^H+\mathbf{U}_{A2}\boldsymbol{\Lambda}_{A2}\mathbf{U}_{A2}^H+\cdots+\mathbf{U}_{Ak}\boldsymbol{\Lambda}_{Ak}\mathbf{U}_{Ak}^H\end{aligned}\tag{10}$$

There is only one principal eigenvalue and several secondary eigenvalues for each $\boldsymbol{\Lambda}_{Ai}, i=1,\cdots,k$ because there is only one dominant scattering mechanism in each SAR SLC image cluster. Therefore, the number of principal eigenvalues of $\hat{\boldsymbol{\Gamma}}_A(p_m)$ is k. Furthermore, since the coherence magnitude of each element in $\hat{\boldsymbol{\Gamma}}_B(p_m)$ is small, the number of principal eigenvalues of $\hat{\boldsymbol{\Gamma}}(p_m)$ can be considered approximately equal to that of $\hat{\boldsymbol{\Gamma}}_A(p_m)$ [33], indicating that all SAR SLC images can be divided into k clusters.

Eigenvalue decomposition is performed of $\hat{\boldsymbol{\Gamma}}(p_m)$. The corresponding number of principal eigenvalues z_m can be estimated using the eigenvalue ratio method or threshold method [3]. $\mathbf{ME}=\begin{bmatrix}z_1 & z_2 & \cdots & z_M\end{bmatrix}^T$ contains the number of principal eigenvalues of M representative pixels, and the mode of $\mathbf{ME}$ is the estimated number of clusters k.

Since the spectral clustering algorithm involves no optimization constraints, it can ensure that the total edge weights within the subgraphs are maximized and that those among the different subgraphs are minimized. In general, the proposed method does not require the coherence of every pair within each cluster to be greater than the coherence of other pairs not involved in the cluster. This guarantees that the total coherence of the interferometric pairs in each cluster is maximized, while that among the different clusters is minimized. Therefore, in the proposed method, low-coherence interferometric pairs are removed, and only high-coherence pairs are retained, which can improve both the quantity and quality of the selected pairs and lay the foundation for high-accuracy interferometric phase estimation.

IV. Experimental Results and Analysis

In this section, the effectiveness of the proposed method is demonstrated using real spaceborne data acquired by the TerraSAR-X and Sentinel-1A satellites for the Beijing International Capital Airport area. The results are compared with those of the threshold method [23] and the graph theory method [29].

A. TerraSAR-X data

The Beijing International Capital Airport is shown in the red box in Fig. 2(a). In total, 33 HH polarization SAR SLC images acquired by the TerraSAR-X satellite from January 22, 2012, to April 10, 2016 are used, with the intensity image acquired on January 22, 2012, as shown in Fig. 2(b).

With the use of the proposed method, the adjacency matrix is constructed first. The combined local frequency and eigenvalue method proposed in [3] is used to detect layover and shadow areas. The strategy proposed in [34] is adopted for detecting water body areas. Candidate pixels are chosen at every 10 pixels along the range and azimuth directions. They are added to the representative pixel set, excluding those in the layover, shadow and water body areas, as well as those whose number of SHPs is larger than or equal to 8. The KS test [8] is used for SHP identification, and the coherence matrix of each representative pixel is estimated based on SHPs, as expressed in (5). By averaging the magnitudes of the coherence matrices of all representative pixels, the estimated coherence matrix of the 33 SAR SLC images can be obtained and employed as the adjacency matrix, as shown in Fig. 3. The coherence value ranges from 0.25~1, significantly varying with the spatial-temporal baseline.

Then, the number of clusters is estimated. Eigenvalue decomposition is performed of the coherence matrix of each representative pixel. The number of principal eigenvalues is estimated by the eigenvalue threshold method [3]. Fig. 4(a) shows the distribution of the number of principal eigenvalues of M representative pixels. The mode of the number of principal eigenvalues is 5. Therefore, the number of clusters is estimated as $k=5$. The normalized Laplacian matrix $\mathbf{D}^{-1/2}\mathbf{L}\mathbf{D}^{-1/2}$ is constructed based on the adjacency matrix, and its eigenvalues are shown in Fig. 4(b). The eigenvalues before the inflection point are considered low eigenvalues, so the number of low eigenvalues is $\alpha=5$ on the basis of Fig. 4(b). Therefore, the dimension of the 33 samples in the feature matrix $\mathbf{F}$ is $k_1=\min(k,\alpha)=5$. Finally, k-means clustering is performed of $\mathbf{F}$ with $k=5$ clusters.

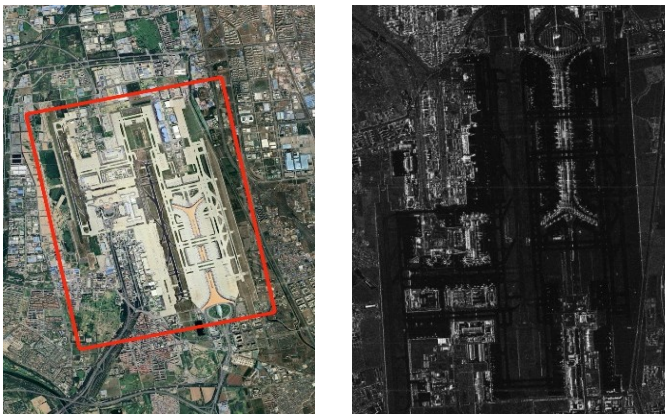

(a) (b)

Fig. 2. TerraSAR-X data: (a) Experimental area; (b) SAR intensity image.

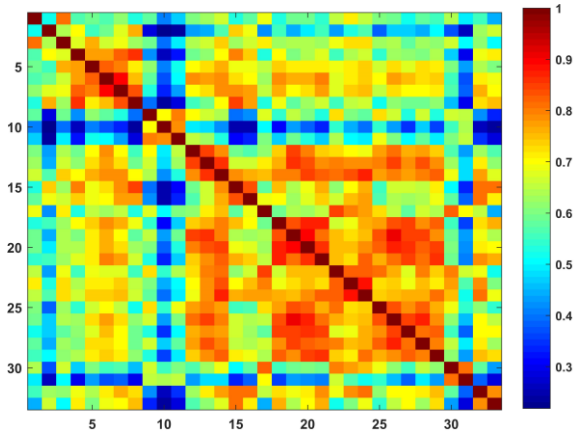

Fig. 3. Estimated coherence matrix of the 33 TerraSAR-X SAR SLC images.

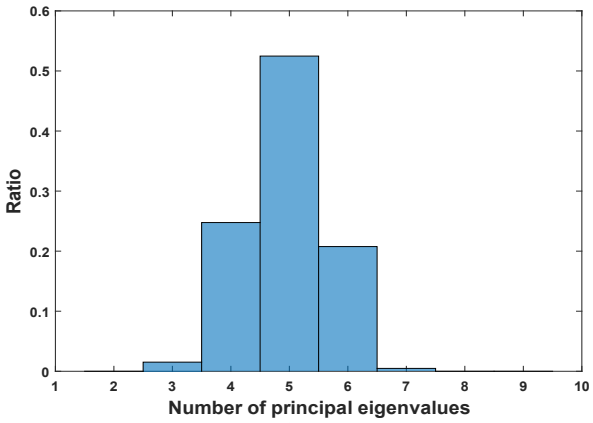

(a)

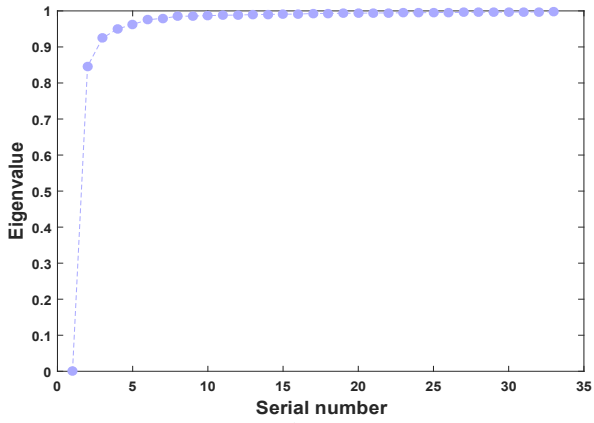

(b)

Fig. 4. Number of clusters of TerraSAR-X data: (a) Distribution of the number of principal eigenvalues of the representative pixels; (b) eigenvalues of the normalized Laplacian matrix.

The coherence spectral clustering results for the 33 SAR SLC images are shown in Fig. 5(a). Each circle in the figure represents an SAR SLC image, and circles of the same color occur in the same cluster. The SAR SLC image acquired on January 22, 2012, is chosen as the first SAR SLC image, and the corresponding spatial-temporal baseline is set as the coordinate origin. In the proposed method, the 33 SAR SLC images are divided into 5 clusters. As shown in Fig. 5(b), any two SAR SLC images in the same cluster can form an interferometric pair, and a total of 118 interferometric pairs are finally selected.

In the threshold method [23], the spatial and temporal baseline thresholds are set to 275 m and 500 days, respectively. In the graph theory method [29], the corridor bridge area of the terminal is chosen to fit the coherence proxy, and the optimization criterion is set to 4, as in [29]. The results are shown in Fig. 6. With the use of the threshold method and graph theory method, 227 and 81 interferometric pairs, respectively, are selected.

To quantitatively evaluate the results, the coherence values of the interferometric pairs selected by the three methods are estimated using the method described in [8]. First, the coherence of each pixel is estimated based on the identified SHPs, and pixels with a coherence greater than 0.5 are then selected; finally, the average coherence of the selected pixels is calculated as the coherence of this interferometric pair. The distributions of the number of selected pairs with respect to coherence obtained by the three methods are given in Table I, where γ denotes the coherence. More detailed coherence distributions of the selected interferometric pairs are shown in Fig. 7.

Although the threshold method results in the largest number of interferometric pairs, there are 13 pairs with coherence values lower than 0.55 because the estimated coherence threshold is too low. In addition, with the use of the threshold method, candidates are selected by setting spatial and temporal baseline thresholds, leading to some high-coherence pairs not being selected at the initial step. For example, the interferometric pair of the 15th and 32nd images is missed due to its large temporal baseline over 700 days. However, this pair still exhibits high coherence and is selected by both the graph theory method and the proposed method.

The graph theory method yields the smallest number of selected pairs. Since the optimization criterion restricts the number of connection lines for each node, this may easily lead to the omission of high-coherence pairs. For example, the coherence between the 13th and 18th SAR SLC images is high; however, the corresponding interferometric pair is missed by the graph theory method but selected by the other two methods.

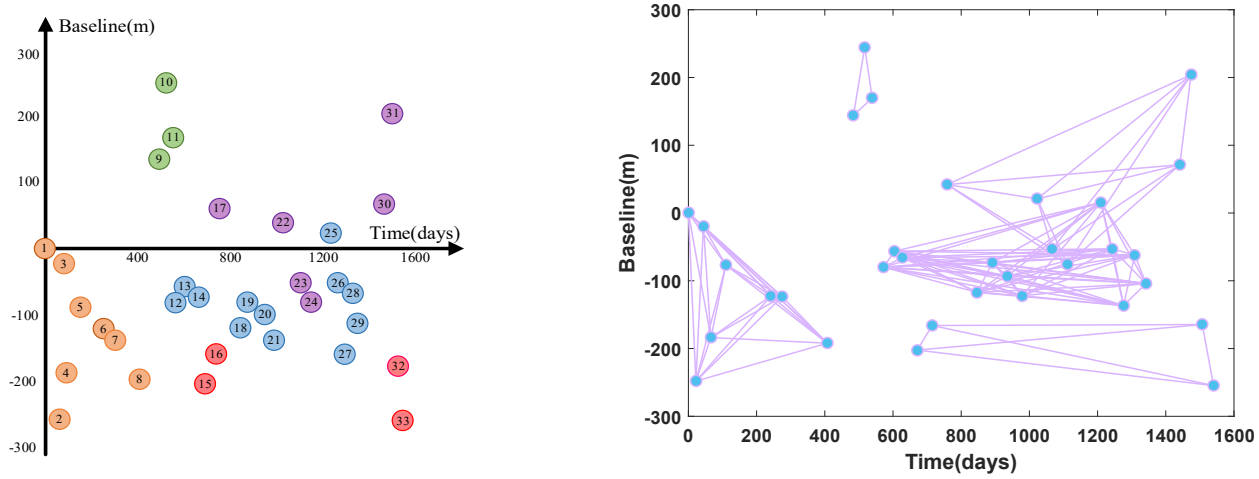

(a) (b)

Fig. 5. Results of the proposed method for the TerraSAR-X data: (a) Coherence spectral clustering results; (b) interferometric pair selection results.

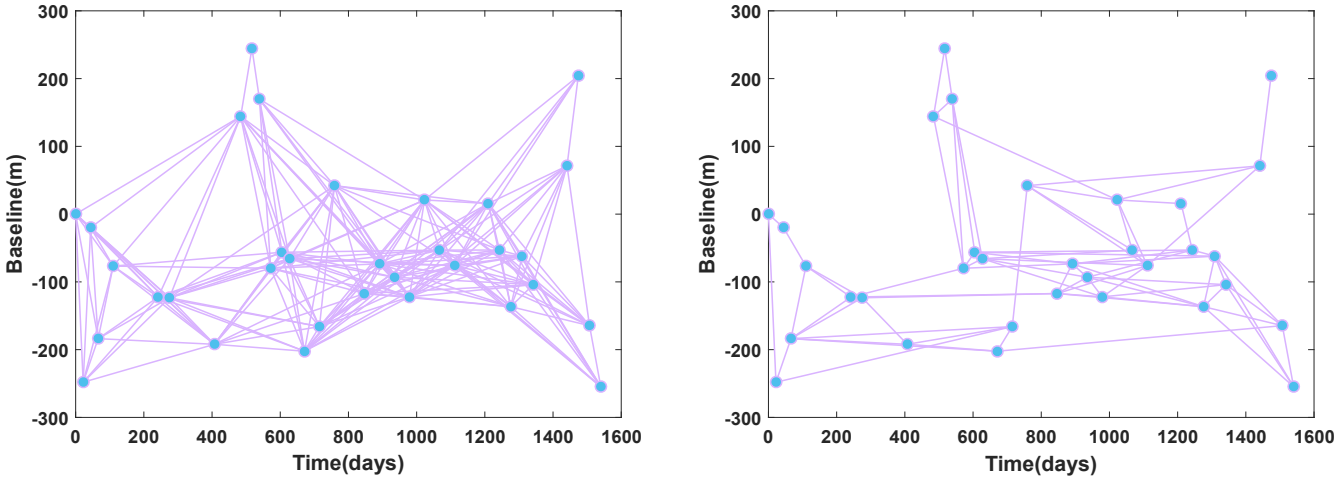

(a) (b)

Fig. 6. Interferometric pair selection results for the TerraSAR-X data: (a) Threshold method; (b) graph theory method.

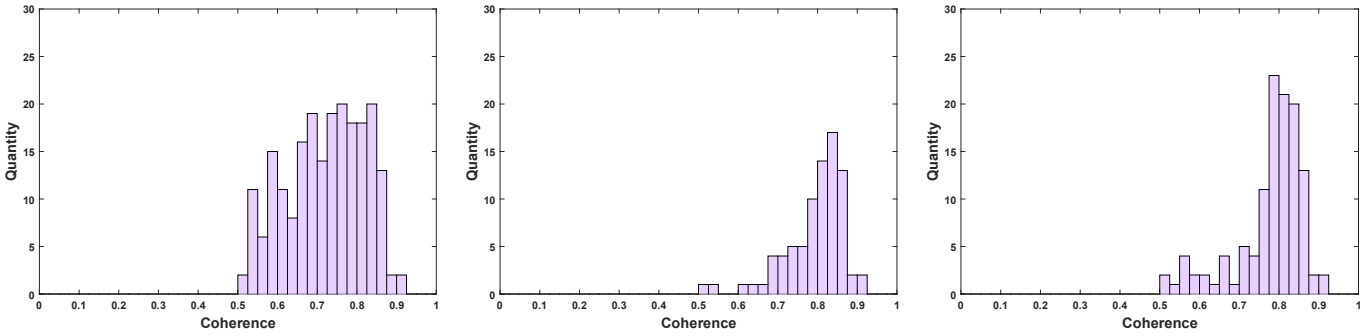

(a) (b) (c)

Fig. 7. Coherence distributions of the selected interferometric pairs for the TerraSAR-X data by (a) the threshold method, (b) the graph theory method, and (c) the proposed method.

TABLE I
COMPARISON OF THE INTERFEROMETRIC PAIRS SELECTED BY THE THREE METHODS FOR THE TERRASAR-X DATA

Method	Number of selected interferometric pairs	$\gamma \in (1, 0.85]$	$\gamma \in (0.85, 0.55]$	$\gamma \in (0.55, 0]$	DEM standard deviation (m)	Average HP standard deviation (mm)
Threshold	214	17	184	13	0.51	1.26
Graph theory	81	17	62	2	0.77	1.73
Proposed	118	17	98	3	0.41	1.17

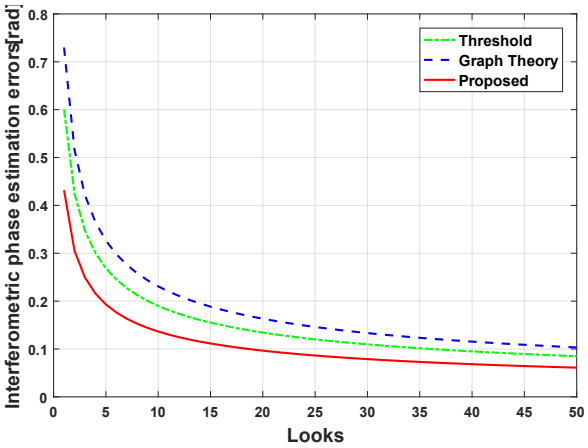

Fig. 8. Interferometric phase estimation CRLBs of the selected interferometric pairs by the three methods for the TerraSAR-X data.

In the proposed method, although the number of selected pairs is smaller than that obtained with the threshold method, the number of pairs with a coherence lower than 0.55 decreases from 13 to 3. Therefore, the proposed method avoids the adverse influence of low-coherence pairs on interferometric phase estimation. Compared with the graph theory method, the number of selected pairs by the proposed method increases as it imposes no constraints. The proposed method yields one more pair with a coherence lower than 0.55 than the graph theory method. However, the proportion of selected pairs with coherence within [0.85,0.55] is much higher than that obtained with the graph theory method.

The coherence matrix of the selected pairs determines the interferometric phase estimation accuracy [18], which directly affects the elevation and deformation measurement accuracy levels. The coherence matrices are generated based on the selection results of the three methods, in which the entries corresponding to the unselected pairs are set to zero and those of the selected ones are set to the corresponding coherence value. To compare the three methods, the CRLBs of phase estimation with the coherence matrices are computed for different looks, as shown in Fig. 8. The CRLB obtained by the proposed method is the lowest because it significantly increases the proportion of high-coherence interferometric pairs and avoids incorrectly selecting low-coherence ones. Therefore, the proposed method can enhance the quality of the coherence matrix and thereby improve the accuracy of interferometric phase estimation.

To further demonstrate the effectiveness of the proposed method, the temporal average coherence of each pixel is calculated, and pixels with a coherence higher than 0.5 are shown in Fig. 9. The number of high-quality pixels with a coherence greater than 0.8 obtained by the proposed method is the largest among the three methods, especially in building areas. This further confirms that the proposed method is more conducive to improving the accuracy of topography and deformation measurements. Then, through the SBAS processing chain [35], the topography and deformation results obtained by the three methods are shown in Fig. 10. Notably, the SBAS method can provide phase values only when the subsets overlap in time [24]. The orange subset, green subset and other subsets do not overlap in time, as shown in Fig. 5(a). Fortunately, many methods have been developed on the basis of the SBAS method to perform deformation retrieval for non-time-overlapped subsets [35]-[37]. The non-time-overlapped subsets are expanded into a large subset by connecting an additional pair with relatively high coherence between the different subsets [35], after which the SBAS method is applied.

Fig. 10 shows that there are obvious differences in the DEMs of the three methods. Focusing on the terminal area, the DEM of the graph theory method significantly differs from those of the other two methods. Due to the lack of externally available real DEM and deformation data, the optical image shown in Fig. 11 is used to quantitatively assess the DEM and deformation results. The eaves in the red box-marked areas of Fig. 11 have a similar height with respect to the ground [38], which are chosen for calculating the DEM standard deviation to assess the DEM smoothness level. The buildings in the white box-marked area of Fig. 11 are rigid structures with similar deformations, so the evaluation strategy proposed in [23] could be adopted for calculating the average high-pass (HP) deformation time-series standard deviation. The evaluation results are listed in Table I. The interferometric pairs selected with the proposed method exhibit the lowest noise in topography estimation and deformation monitoring, as indicated by the smallest DEM standard deviation and average HP standard deviation.

B. Sentinel-1A Dual Polarization Data

To assess the performance of the proposed method on dual polarization data, a set of Sentinel-1A dual polarization data is used to conduct the experiment. Regarding the Beijing Capital International Airport, 38 SAR SLC images acquired by the Sentinel-1A satellite from August 5, 2016, to December 22, 2017, are chosen, including 19 VV and 19 VH SAR SLC images. The VV and VH images acquired on August 5, 2016, are shown in Fig. 12.

First, the proposed method is applied. The estimated coherence matrix of the 38 SAR SLC images is shown in Fig. 13, in which the first 19 are VV polarization images and the last 19 are VH polarization images. The coherence matrices of the images with different polarizations are different even with the same spatial-temporal baseline. Moreover, the coherence between the SAR SLC images with different polarizations is very low.

Then, the number of clusters is estimated. The same method and parameters as those in the TerraSAR-X data experiment are used here. The distribution of the number of principal eigenvalues of M representative pixels and the eigenvalues of the normalized Laplacian matrix are shown in Fig. 14. The estimated number of clusters is $k=4$, and the number of low eigenvalues is $\alpha=4$, so $k_1=\min(k,\alpha)=4$.

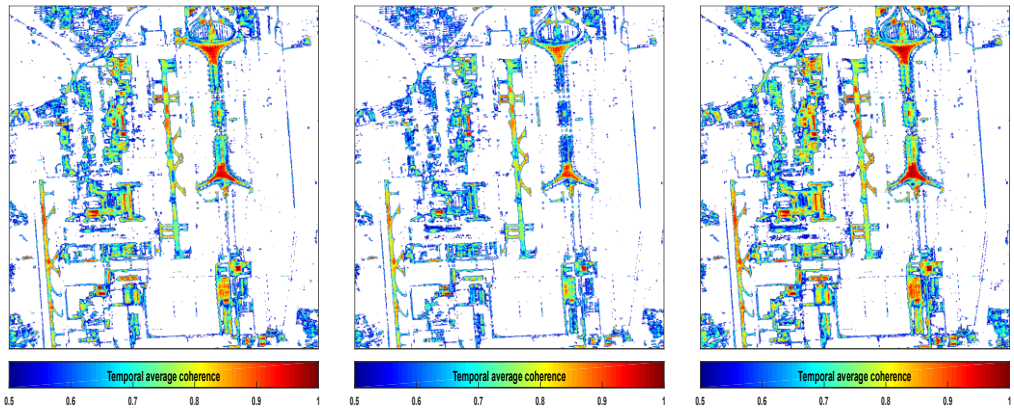

(a) (b) (c)

Fig. 9. Temporal average coherence maps of TerraSAR-X data by (a) the threshold method, (b) the graph theory method, and (c) the proposed method. The number of high-quality pixels with temporal average coherence greater than 0.8 of (a) the threshold method, (b) the graph theory method, and (c) the proposed method is 24985, 13826 and 33510, respectively.

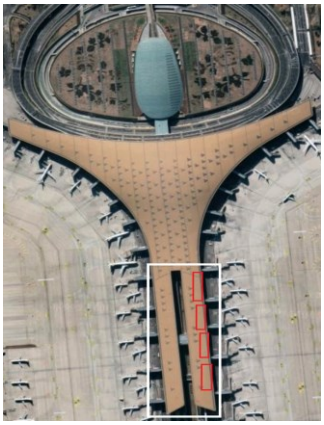

Fig. 11. Optical image of the terminal area.

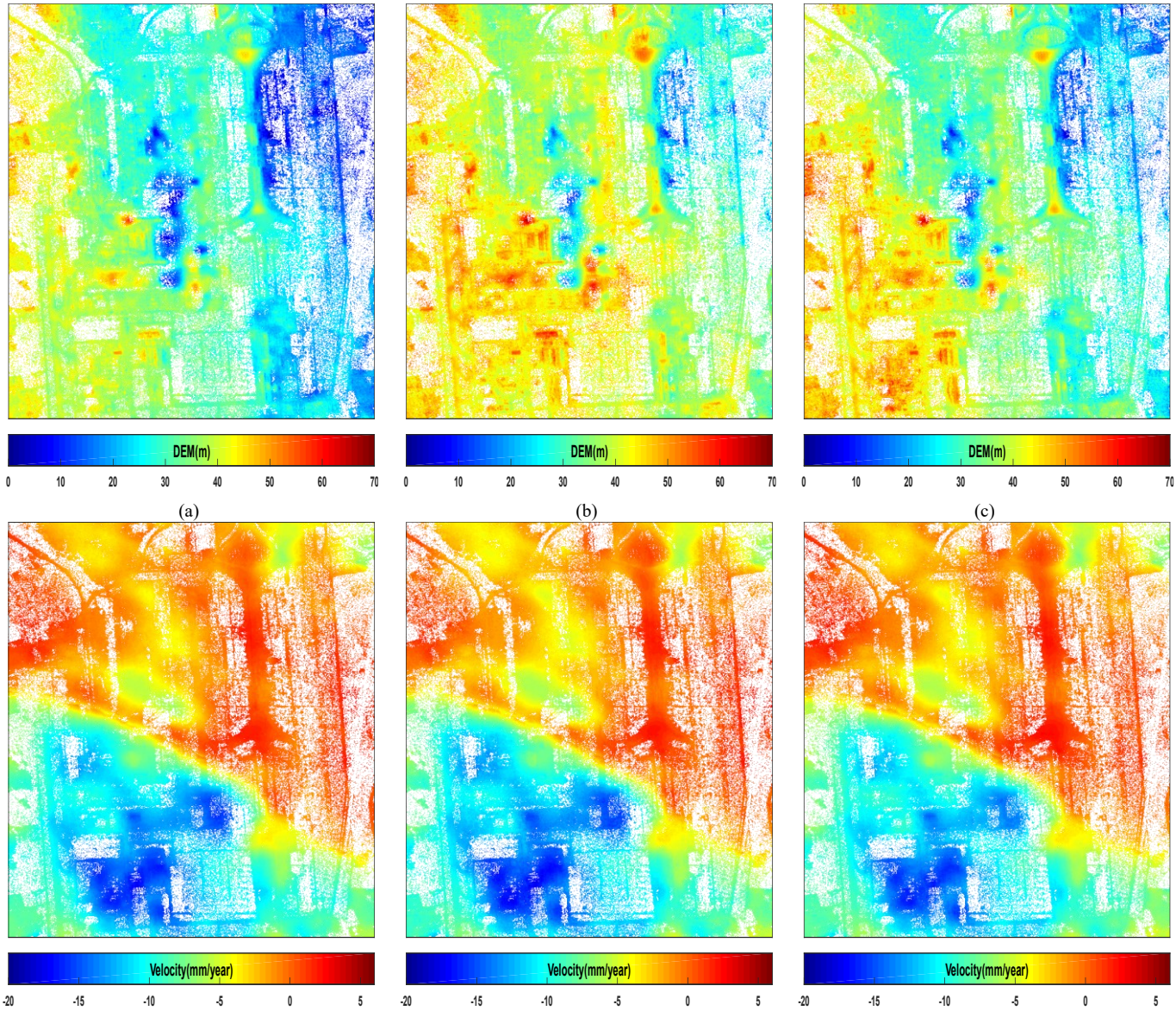

(a) (b) (c) (d) (e) (f)

Fig. 10. Topography and deformation results for the TerraSAR-X data by the DEM obtained with (a) the threshold method, (b) the graph theory method, and (c) the proposed method; (d) deformation velocity map obtained with the threshold method; (e) deformation velocity map obtained with the graph theory method; (f) deformation velocity map obtained with the proposed method.

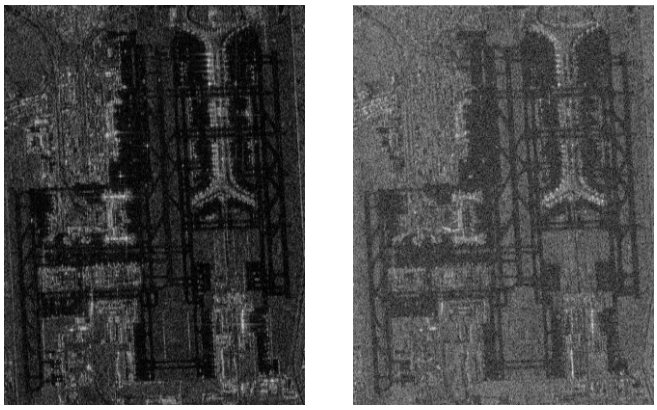

(a) (b)

Fig. 12. Sentinel-1A dual polarization SAR intensity images: (a) VV polarization; (b) VH polarization.

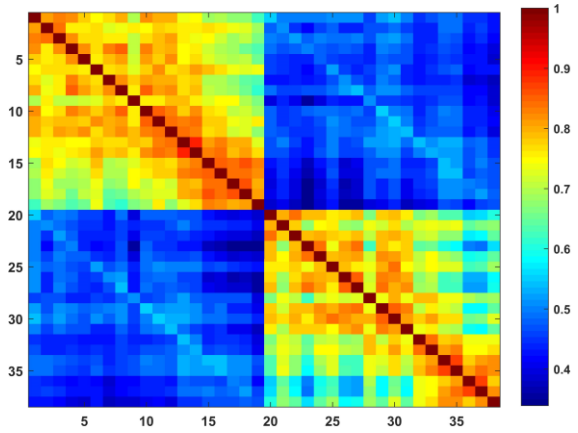

Fig. 13. Estimated coherence matrix of the 38 Sentinel-1A dual polarization SAR SLC images.

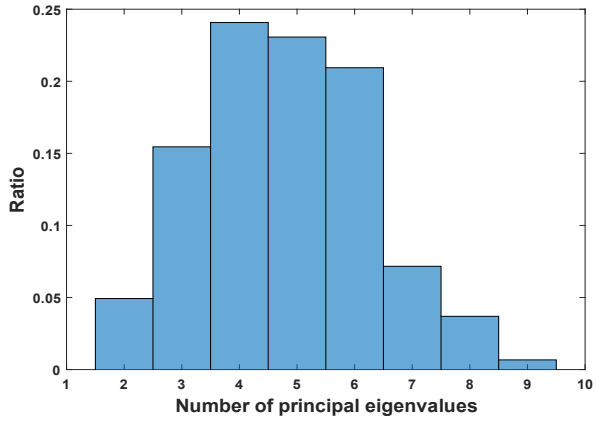

(a)

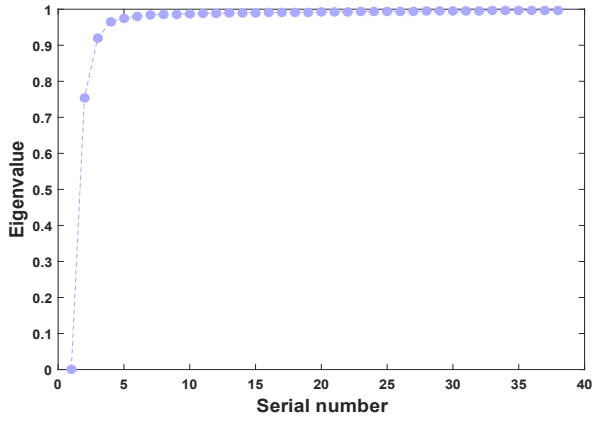

(b)

Fig. 14. Estimation results of the number of clusters for the Sentinel-1A dual polarization data: (a) Distribution of the number of principal eigenvalues of the representative pixels; (b) eigenvalues of the normalized Laplacian matrix.

In this experiment, the VV and VH SAR SLC images are almost uncorrelated, so clustering is independently conducted of the VV and VH SAR SLC images. The clustering results are shown in Fig. 15(a) and (b), respectively. The corresponding selection results are shown in Fig. 15(c) and (d), respectively. Notably, 87 and 83 interferometric pairs are selected from the VV and VH SAR SLC images, respectively.

Regarding the threshold method [23], the temporal and spatial baseline thresholds are set to 500 days and 250 m, respectively. In the graph theory method [29], the corridor bridge area is also chosen to fit the coherence proxy, and the optimization criterion is set to 4 [29]. The results of the threshold method are shown in Fig. 16(a) and (b), where there are 63 and 36 interferometric pairs selected for the VV and VH polarization images, respectively. The results of the graph theory method are shown in Fig. 16(c) and (d), and 59 interferometric pairs are selected for both the VV and VH polarization images.

The quantitative evaluation results for the coherence of the selected pairs are provided in Table II and Fig. 17. The coherence of each pair is calculated by averaging the coherence of the selected pixels with a coherence greater than or equal to 0.5. The distributions of the number of selected pairs with respect to coherence obtained with the three methods are listed in Table II. Fig. 17 shows more specific coherence distributions of the selected pairs.

When using the threshold method, the number of selected pairs is highly sensitive to the threshold. A high threshold will reduce the number of selected pairs and result in high-coherence interferometric pairs not being selected. However, a low threshold may lead to some low-coherence pairs being wrongly selected. As indicated in Table II and Fig. 17(d), only 36 interferometric pairs are selected from the VH polarization images. The coherence threshold in the VH polarization images is very high, resulting in the omission of many high-coherence pairs. For example, the coherence between the 1st and 5th VH polarization SAR SLC images reaches 0.7875, while the corresponding pair is not selected in the threshold method but selected by the other two methods.

The graph theory method is limited by the usage of each SAR SLC image as either a primary or secondary image. As a result, only 59 interferometric pairs are selected from both the VV and VH polarization images. Fig. 15(c) and Fig. 16(a) and (c) show that the 7th and 12th VV polarization SAR SLC images are not connected in the graph theory method because of inappropriate constraints. In contrast, this pair is selected with the threshold method and the proposed method given its high coherence.

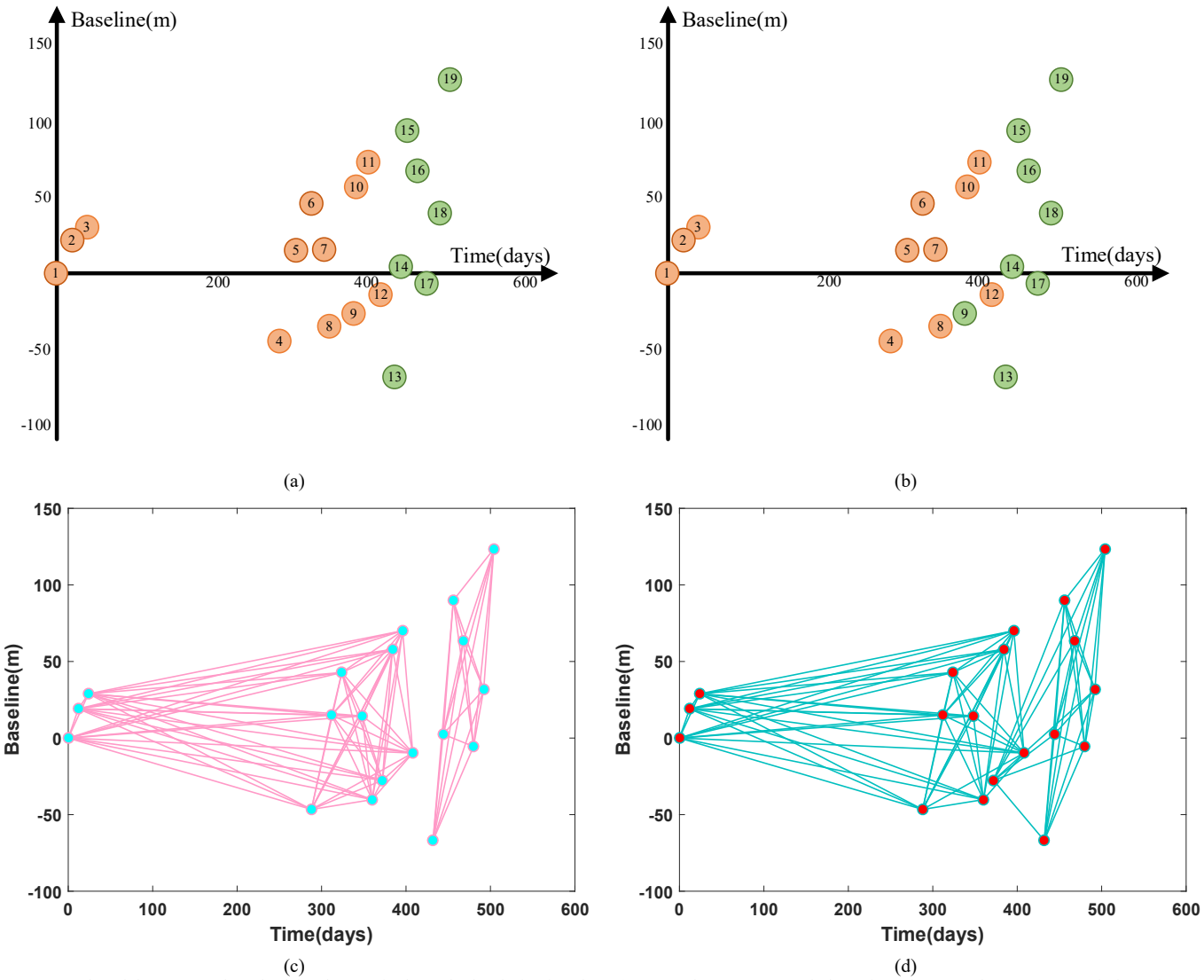

Fig. 15. Results of the proposed method for the Sentinel-1A dual polarization data: (a) VV coherence spectral clustering; (b) VH coherence spectral clustering; (c) VV interferometric pair selection; (d) VH interferometric pair selection.

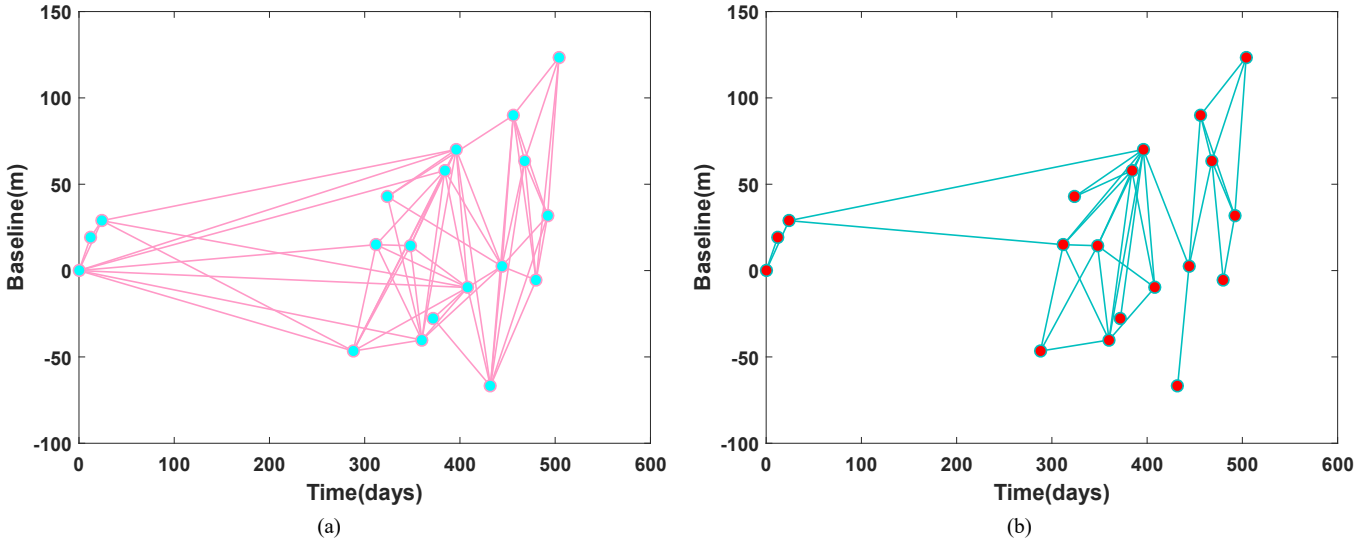

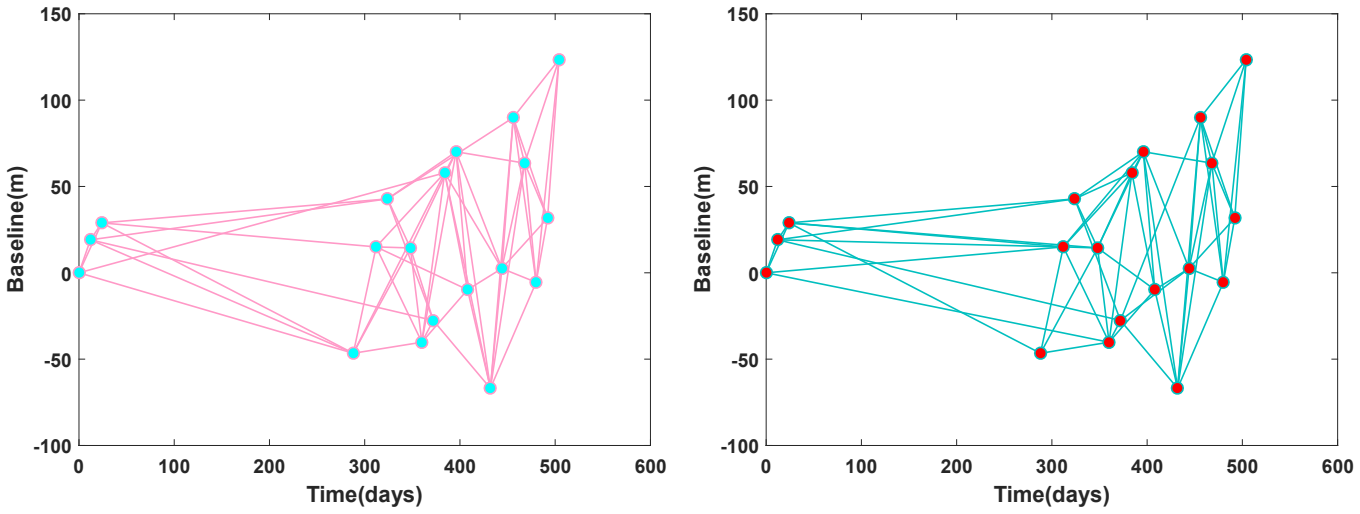

(c) (d)

Fig. 16. Selection results for the Sentinel-1A dual polarization data: (a) VV with the threshold method; (b) VH with the threshold method; (c) VV with the graph theory method; (d) VH with graph theory method.

TABLE II
COMPARISON OF THE INTERFEROMETRIC PAIRS SELECTED BY THE THREE METHODS FOR THE SENTINEL-1A DUAL POLARIZATION DATA

Polarization	Method	Number of selected interferometric pairs	$\gamma \in (1, 0.85]$	$\gamma \in (0.85, 0.55]$	$\gamma \in (0.55, 0]$	DEM standard deviation (m)	Average HP standard deviation (mm)
VV	Threshold	63	4	59	0	1.47	0.71
	Graph theory	59	4	55	0	1.89	0.74
	Proposed	87	4	83	0	1.32	0.69
VH	Threshold	36	3	33	0	2.20	1.03
	Graph theory	59	3	56	0	2.14	1.01
	Proposed	83	3	80	0	1.65	0.98

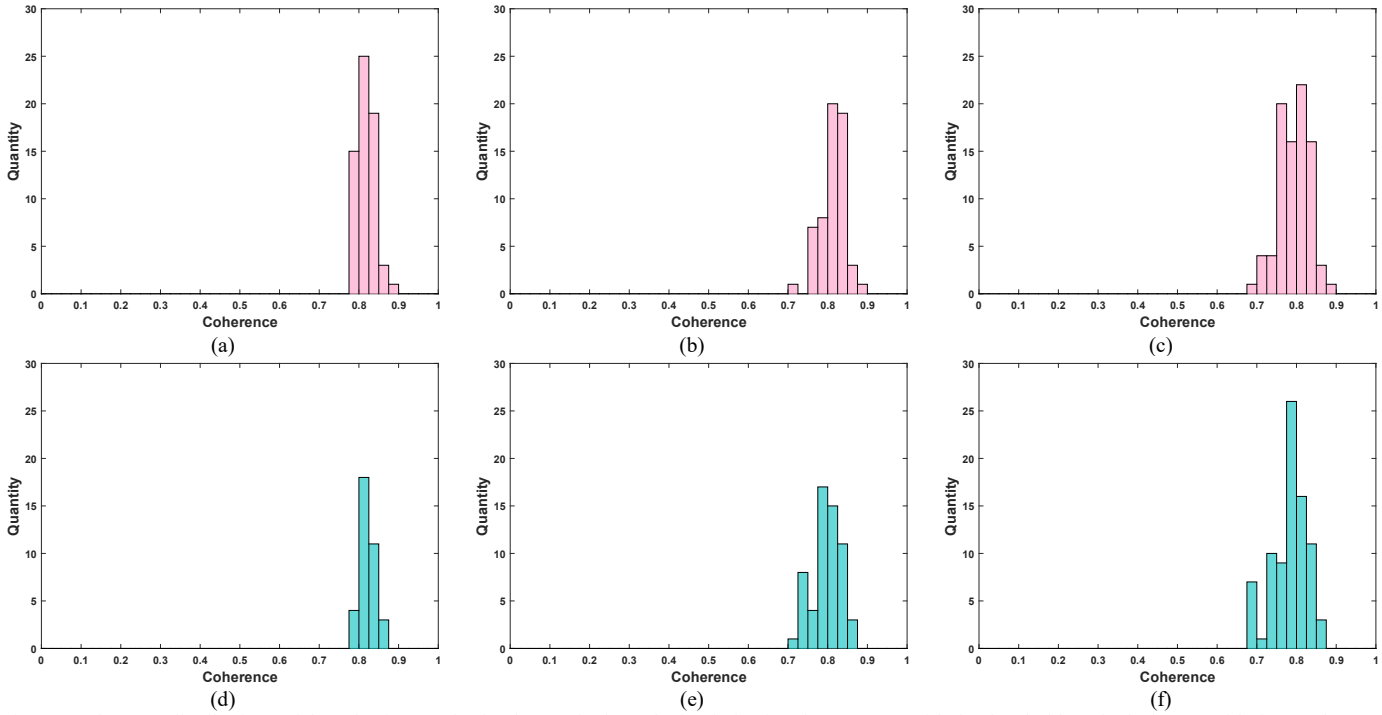

(a) (b) (c)

(d) (e) (f)

Fig. 17. Coherence distributions of the selection results for the Sentinel-1A dual polarization data: (a) VV with the threshold method; (b) VV with the graph theory method; (c) VV with the proposed method; (d) VH with the threshold method; (e) VH with the graph theory method; (f) VH with the proposed method.

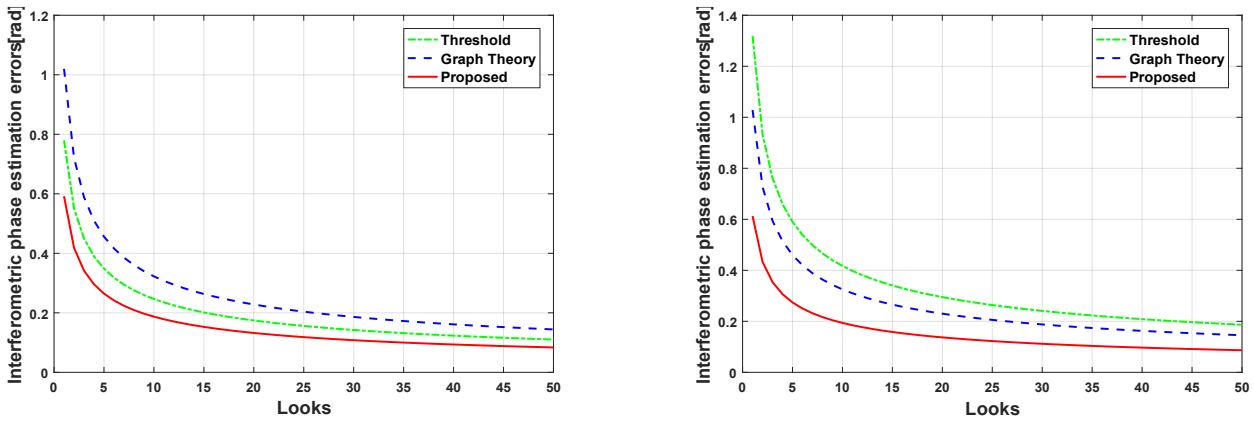

Fig. 18. Interferometric phase estimation CRLBs of the selected interferometric pairs for the Sentinel-1A dual polarization data: (a) VV polarization; (b) VH polarization.

Compared with the other two methods, the proposed method can not only remove low-coherence pairs but also ensure that high-coherence pairs are selected. For example, the coherence between the 1st and 7th SAR SLC images of the VV and VH polarization images are 0.7655 and 0.7717, respectively. The corresponding pairs are selected by the proposed method but missed by the other two methods.

To further evaluate the influence of the selection results on interferometric phase estimation, the phase estimation CRLBs of the selected pairs for different looks are shown in Fig. 18. The threshold method is superior to the graph theory method for VV polarization data, while the graph theory method is better than the threshold method for VH polarization data. In both the VV and VH cases, the CRLBs of the proposed method are the lowest.

Moreover, for the selected interferometric pairs, the number of high-quality pixels with a temporal average coherence greater than 0.8 is calculated. The results of the threshold method, graph theory method and proposed method for the VV polarization data are 27133, 20827 and 27784, respectively. For the VH polarization data, the results of the threshold method, graph theory method and proposed method are 6613, 7986 and 10302, respectively. Then, the SBAS processing chain [35] is implemented to obtain topography and deformation results. The evaluation results for the white and red box-marked areas in Fig. 11 are listed in Table II. For the two types of polarization data, the DEM standard deviation and average HP standard deviation obtained with the proposed method are the smallest among the three approaches, which indicates that the interferometric pairs selected by the proposed method can provide the most accurate and robust topography and deformation results.

In summary, it is demonstrated that the sensitivity of the different polarization data to scene feature properties differs [39]. Therefore, even with the same spatial-temporal baseline, the coherence of pairs with different polarizations can still differ, leading to deviations in the selection results. The threshold method requires an appropriate coherence threshold, which is hard to define. The number of selected pairs, which in turn affects the accuracy of interferometric phase estimation, is directly influenced by the coherence threshold. The graph theory method limits the number of connection lines for each node, which may lead to the omission of high-coherence interferometric pairs. Therefore, the interferometric phase estimation accuracy of the graph method is affected by the constraints. By combining coherence and spectral clustering, the proposed method does not impose such constraints. It can account for both the coherence level and the number of selected pairs, thus removing low-coherence interferometric pairs and providing as many high-quality pairs as possible. As a result, the estimation accuracy of the proposed method is higher than that of the other two methods.

V. Conclusions

In this paper, a novel method for selecting SAR interferometric pairs is proposed. To accurately characterize the coherence between two SAR SLC images, representative pixels are chosen, and their coherence matrices are estimated by detecting SHPs. The adjacency matrix, which can reflect the similarity between any two SAR SLC images, is constructed by averaging the coherence matrices of all representative pixels. Then, the number of clusters is estimated by performing eigenvalue decomposition of the coherence matrix of each representative pixel. Finally, based on the constructed adjacency matrix and the estimated number of clusters, coherence spectral clustering is performed of SAR SLC images. The aim is to ensure that the total coherence of the interferometric pairs in the same cluster is maximized while that among the different clusters is minimized. Therefore, the proposed method provides a higher proportion of high-coherence interferometric pairs and avoids the selection of low-coherence pairs. As demonstrated by the experimental results using real data, the proposed method can improve the quality of the coherence matrix and subsequently achieve more accurate interferometric phase estimation.

It should be noted that empirical parameters are used in the proposed method. For example, the equal-interval parameter and the number of SHPs parameter for selecting representative pixels, as well as the parameter for determining the number of principal eigenvalues of representative pixels. These empirical

parameters affect the estimation accuracy of the coherence matrix and the number of clusters and thus indirectly affect the selection results. In fact, the empirical parameters used in existing selection methods directly or indirectly affect the selection results. Therefore, how to reduce their adverse effects on the selection results should be further studied in subsequent research.

REFERENCES

[1] G. Krieger et al., "TanDEM-X: A Satellite Formation for High-Resolution SAR Interferometry," *IEEE Transactions on Geoscience and Remote Sensing*, vol. 45, no. 11, pp. 3317-3341, Nov. 2007.

[2] P. A. Rosen et al., "Synthetic aperture radar interferometry." *Proceedings of the IEEE*, vol. 88, no. 3, pp. 333-382, 2000.

[3] H. Xu et al., "Multibaseline InSAR Layover Detection Based on Local Frequency and Eigenvalue," *IEEE Journal of Selected Topics in Applied Earth Observations and Remote Sensing*, vol. 14, pp. 10571-10582, 2021.

[4] G. Ferraioli, C. A. Deledalle, L. Denis and F. Tupin, "Parisar: Patch-Based Estimation and Regularized Inversion for Multibaseline SAR Interferometry," *IEEE Transactions on Geoscience and Remote Sensing*, vol. 56, no. 3, pp. 1626-1636, Mar. 2018.

[5] C. Wang et al., "A New Likelihood Function for Consistent Phase Series Estimation in Distributed Scatterer Interferometry," *IEEE Transactions on Geoscience and Remote Sensing*, vol. 60, pp. 1-14, 2022, Art no. 5227314.

[6] A. Pepe, P. Mastro and C. E. Jones, "Adaptive Multilooking of Multitemporal Differential SAR Interferometric Data Stack Using Directional Statistics," *IEEE Transactions on Geoscience and Remote Sensing*, vol. 59, no. 8, pp. 6706-6721, Aug. 2021.

[7] W. Zhang et al., "Improved DEM Reconstruction Method Based on Multibaseline InSAR," *IEEE Geoscience and Remote Sensing Letters*, vol. 19, pp. 1-5, 2022, Art no. 4011505.

[8] A. Ferretti, A. Fumagalli, F. Novali, C. Prati, F. Rocca and A. Rucci, "A New Algorithm for Processing Interferometric Data-Stacks: SqueeSAR," *IEEE Transactions on Geoscience and Remote Sensing*, vol. 49, no. 9, pp. 3460-3470, Sept. 2011.

[9] G. Fornaro, S. Verde, D. Reale and A. Pauciullo, "CAESAR: An Approach Based on Covariance Matrix Decomposition to Improve Multibaseline–Multitemporal Interferometric SAR Processing," *IEEE Transactions on Geoscience and Remote Sensing*, vol. 53, no. 4, pp. 2050-2065, Apr. 2015.

[10] H. Ansari, F. De Zan, and R. Bamler, "Efficient phase estimation for interferogram stacks," *IEEE Transactions on Geoscience and Remote Sensing*, vol. 56, no. 7, pp. 4109–4125, Jul. 2018.

[11] P. Berardino, G. Fornaro, R. Lanari and E. Sansosti, "A new algorithm for surface deformation monitoring based on small baseline differential SAR interferograms," *IEEE Transactions on Geoscience and Remote Sensing*, vol. 40, no. 11, pp. 2375-2383, Nov. 2002.

[12] N. Cao, H. Lee and H. C. Jung, "Mathematical Framework for Phase-Triangulation Algorithms in Distributed-Scatterer Interferometry," *IEEE Geoscience and Remote Sensing Letters*, vol. 12, no. 9, pp. 1838-1842, Sept. 2015.

[13] N. Cao, H. Lee and H. C. Jung, "A Phase-Decomposition-Based PSInSAR Processing Method," *IEEE Transactions on Geoscience and Remote Sensing*, vol. 54, no. 2, pp. 1074-1090, Feb. 2016.

[14] H. Ansari, F. De Zan and R. Bamler, "Sequential Estimator: Toward Efficient InSAR Time Series Analysis," *IEEE Transactions on Geoscience and Remote Sensing*, vol. 55, no. 10, pp. 5637-5652, Oct. 2017.

[15] A. Sowter et al., "DInSAR estimation of land motion using intermittent coherence with application to the South Derbyshire and Leicestershire coalfield," *Remote Sensing Letters*, vol. 4, no. 10, pp. 979-987, Oct. 2013.

[16] S. V. Samsonov and N. d'Oreye, "Multidimensional small baseline subset (MSBAS) for two-dimensional deformation analysis: Case study Mexico City," *Canadian Journal of Remote Sensing*, vol. 43, no. 4, pp. 318–329, Jul. 2017.

[17] F. Casu et al., "Deformation Time-Series Generation in Areas Characterized by Large Displacement Dynamics: The SAR Amplitude Pixel-Offset SBAS Technique," *IEEE Transactions on Geoscience and Remote Sensing*, vol. 49, no. 7, pp. 2752-2763, July 2011.

[18] A. M. Guarnieri and S. Tebaldini, "On the Exploitation of Target Statistics for SAR Interferometry Applications," *IEEE Transactions on Geoscience and Remote Sensing*, vol. 46, no. 11, pp. 3436-3443, Nov. 2008.

[19] A. Ferretti, C. Prati and F. Rocca, "Permanent scatterers in SAR interferometry," *IEEE Transactions on Geoscience and Remote Sensing*, vol. 39, no. 1, pp. 8-20, Jan. 2001.

[20] F. Falabella et al., "On the Use of Weighted Least-Squares Approaches for Differential Interferometric SAR Analyses: The Weighted Adaptive Variable-lEngth (WAVE) Technique," *Sensors*, vol. 20, no. 4, p. 1103, Feb. 2020.

[21] K. Ishitsuka, T. Tsuji, and T. Matsuoka, "Pixel-based interferometric pair selection in InSAR time-series analysis with baseline criteria," *Remote Sensing Letters*, vol. 7, no.7, pp. 711-720, 2016.

[22] H. Wu et al., "Semi-automatic selection of optimum image pairs based on the interferometric coherence for time series SAR interferometry," *Remote Sensing Letters*, vol. 10, no.11, pp. 1105-1112, 2019.

[23] B. Wang et al., "Analysis of groundwater depletion/inflation and freeze–thaw cycles in the Northern Urumqi region with the SBAS technique and an adjusted network of interferograms," *Remote Sensing*, vol. 13, no. 11, p. 2144, May 2021.

[24] A. Pepe et al., "Improved EMCF-SBAS Processing Chain Based on Advanced Techniques for the Noise-Filtering and Selection of Small Baseline Multi-Look DInSAR Interferograms," *IEEE Transactions on Geoscience and Remote Sensing*, vol. 53, no. 8, pp. 4394-4417, Aug. 2015.

[25] M. Jiang and A. M. Guarnieri, "Distributed Scatterer Interferometry with the Refinement of Spatiotemporal Coherence," *IEEE Transactions on Geoscience and Remote Sensing*, vol. 58, no. 6, pp. 3977-3987, June 2020.

[26] Z. Gao et al., "FCSN 3-D PU: Fully Connected Spatiotemporal Network Based 3-D Phase Unwrapping," *IEEE Geoscience and Remote Sensing Letters*, vol. 20, pp. 1-5, 2023, Art no. 4003605.

[27] H. Liang, L. Zhang and X. Li, "Enhancing MTInSAR Phase Unwrapping in Decorrelating Environments by Spatiotemporal Observation Optimization," *IEEE Geoscience and Remote Sensing Letters*, vol. 20, pp. 1-5, 2023, Art no. 4002505.

[28] M. Jiang. "Sentinel-1 TOPS co-registration over low-coherence areas and its application to velocity estimation using the all pairs shortest path algorithm," *Journal of Geodesy*, vol. 94, no. 10, p. 95, Sep. 2020.

[29] D. Smittarello et al., "Pair selection optimization for InSAR time series processing." *Journal of Geophysical Research: Solid Earth*, vol. 127, no. 3, p. e2021JB022825, Mar. 2022.

[30] U. Von Luxburg, "A tutorial on spectral clustering." *Statistics and computing*, vol. 17, no. 4, pp. 395-416, Dec. 2007.

[31] J. Shi and J. Malik, "Normalized cuts and image segmentation," *IEEE Transactions on Pattern Analysis and Machine Intelligence*, vol. 22, no. 8, pp. 888-905, Aug. 2000.

[32] S. Navneet, J. W. Kim and Z. Lu, "A New InSAR Persistent Scatterer Selection Technique Using Top Eigenvalue of Coherence Matrix," *IEEE Transactions on Geoscience and Remote Sensing*, vol. 56, no. 4, pp. 1969-1978, Apr. 2018.

[33] G H. Golub, C F. Van Loan. "Matrix computations". JHU press, 2013.

[34] U. Soergel et al. "Feature Extraction and Visualization of Bridges Over Water From High-Resolution InSAR Data and One Orthophoto," *IEEE Journal of Selected Topics in Applied Earth Observations and Remote Sensing*, vol. 1, no. 2, pp. 147-153, June 2008.

[35] J. Hu et al, "Spatial-temporal surface deformation of Los Angeles over 2003-2007 from weighted least squares DInSAR," *International Journal of Applied Earth Observation and Geoinformation*, vol. 21, pp. 484–492, Apr. 2013.

[36] A. Pepe et al., "The Use of C-/X-Band Time-Gapped SAR Data and Geotechnical Models for the Study of Shanghai's Ocean-Reclaimed Lands through the SBAS-DInSAR Technique," *Remote Sensing*, vol. 8, no. 11, p. 911, Nov. 2016.

[37] Y. Liu et al., "A constrained small baseline subsets (CSBAS) InSAR technique for multiple subsets," *European Journal of Remote Sensing*, vol. 53, no. 1, pp. 14-26, May 2020.

[38] B. Yang et al., "Realistic Lower Bound on Elevation Estimation for Tomographic SAR," *IEEE Journal of Selected Topics in Applied Earth Observations and Remote Sensing*, vol. 11, no. 7, pp. 2429-2439, July 2018.

[39] J. Luo, et al. "Assessment of the Contribution of Polarimetric Persistent Scatterer Interferometry on Sentinel-1 Data," *IEEE Journal of Selected Topics in Applied Earth Observations and Remote Sensing*, vol. 15, pp. 7997-8009, 2022.